PNAS
www.pnas.org

Supplementary Information for

Munc13 structural transitions and oligomers that may choreograph successive stages in vesicle priming for neurotransmitter release

Kirill Grushin, R. Venkat Kalyana Sundaram, Charles V. Sindelar[1], and James E. Rothman[2]

Email: 1. charles.sindelar@yale.edu
2. james.rothman@yale.edu

This PDF file includes:

Supplementary text
Figures S1 to S13
Legends for Movies S1 to S2
SI References

Other supplementary materials for this manuscript include the following:

Movies S1 to S2

Supplementary Information Text

Materials and Methods.

Image processing and tomogram reconstruction

For the first (Glacios) dataset, tilt movies were aligned using MotionCor2 (1) and tilts were saved as mrc stacks using *alignframes* from the IMOD software package (2). The resulting tilt series were aligned using IMOD by tracking fiducial markers. For the crystal quality evaluation each tomogram was reconstructed in IMOD from 4x binned non-CTF-corrected tilt series using the Simultaneous Iterative Reconstruction Technique (SIRT) (3). A total of 10 tomograms were selected for further data processing. Obtained tilt series alignment parameters were transferred to the emClarity (4) framework. To create an initial model for automatic particle picking in the emClarity pipeline, one tomogram was used for manual selection of 614 particles centered within visible hexagons. These subtomograms were aligned and averaged without applied symmetry over three iterations using IMOD/PEET software ((5) http://bio3d.colorado.edu/PEET). A hexagonal segment of the resulting 3D volume (figure) unit was used for template matching particle picking in emClarity. The template matching results were cleaned manually and a total of 5467 subtomograms were used for further alignment and averaging with gradual binning reduction of 4x, 2x and 1x (we followed the published protocol (4) and available tutorial (https://github.com/ffyr2w/emClarity-tutorial/) but omitted the TomoCPR steps). C6 symmetry was applied throughout all averaging procedures. Resolution of final 3D volume was calculated by the gold standard method.

For the final (Krios) dataset, the tilt series were processed using Warp 1.0.9 software (6). Super-resolution movies of individual tilts were 2x binned (resulting in pixel size of 2.1Å) and aligned along with defocus estimation. After this step poor-quality tilt images (shifted from original area, blocked by contamination at higher tilts etc.) were removed. Tilt series were exported from WARP and aligned in IMOD using gold fiducial markers at 4x binned pixel size. Tomograms with a residual error higher than 0.8 within a 4x binned pixel (~6.7 Å) or with fewer than 5 fiducials were discarded. Alignment parameters were used in Warp to create final, exposure-filtered tilt series stacks along with whole tilt-series defocus estimations. For template matching, we segmented the hexagonal element of the 3D volume reconstructed from the Glacios dataset. The volume was bandpass filtered to 40 Å and used for template matching in the 6x binned tomograms (12.6 Å/pixel). The resulting cross-correlation maps

were manually checked using the Cube program (https://github.com/dtegunov/cube) and false-positives or locations clearly outside the visible hexagonal network were discarded. The remaining particle coordinates were used for subtomogram extraction with 80 pixels box size at 12.6 Å/pixel. In total,36,837 subtomograms and the corresponding 3D CTF/wedge models were transferred into Relion 3.1 (7, 8).

Multiple rounds of RELION 3D classification and 3D refinement were performed with subsequent re-extraction of subtomograms within Warp with reduced pixel size binning (6x, 4x, 2x, 1x) (Figure S13). The final dataset of 12,149 particles at 2.1 Å/pixel and 196 voxels size was refined with a focus on protein molecules composing the inner hexagonal unit (6 lateral molecules adjacent to 6 upright Munc13L molecules) by using a mask encompassing this region (Figure S12). The resulting 3D reconstruction was postprocessed with the same region used during refinement. The estimated resolution using gold-standard method was 12.5Å at the 0.143 criterion. Next using M (9), the tilt series were refined using image warp with a 6x4 grid and volume warp with 2x3x2x10 grid. Particle poses and angles were refined for one temporal sampling point. Subtomograms were re-extracted from the refined tilt-series and aligned again in RELION 3D refine. RELION post-processing was applied to the resulting half-maps and applied empirically derived B-factor of -600. The mask used for post-processing was similar to the one used previously which encompassed the central hexagonal unit. The estimated resolution of the region within the mask was 10 Å.

Local resolution estimation (Fig. S2C) showed that the 3D map is better resolved in the middle of the crystal: densities positioned closer to lipid membranes and beyond the central hexagon area resolved poorly likely due to flexibility of the crystal. To address this problem and better resolve the trimer of upright Munc13L molecules, we repeated the template matching process in Warp using the triradiate crystal segment with a trimer in the center (Fig. S13). After manual selection, the resultant dataset of 70,467 subtomograms was processed similarly except at all steps C3 symmetry was used. Final 3D refinement of the selected 42,237 subtomograms at 2.1A/pix and 192 voxels size was focused on the Munc13L trimer by applying a mask around it. The resultant structure was refined in M using the same parameters as the hexagons. The resolution 10.4Å of the refined volume was estimated within M using the gold standard method at 0.143 criterion. Second, we applied symmetry expansion to both datasets with subsequent 3D classification without any alignment of the single asymmetric unit of the crystal. Briefly, by using *relion_particle_symmetry_expand* program each hexagon or trimer particle was rotated around a symmetry axis (six or three times correspondingly) thus expanding

the particle data set where each element of the crystal is at the same position. This allowed us to implement masked classification of selected regions without angular searches. After multiple rounds of 3D classification, the best classes were used for structural analysis and flexible fitting (Fig. S3, S13). We did not perform 3D refinement of those final classes. In our hands, all attempts at running 3D refine with only local angular searches of the expanded particles set resulted in 3D reconstructions with no resolution improvement or worse than original symmetrized 3D volume probably due to the problems with the alignment of relatively small (around or less than 130 kDa) structural elements within the masked area.

Model fitting, data analysis

All 3D volume segmentations were performed in UCSF Chimera (10).
Rigid body fitting was performed using *Fit in map* function in Chimera. The models used for fitting included C1C2BMUN (pdb:5UE8), Ca^{++}bound Munc13-1 C2B domain (pdb:6NYT), MUN domain crystal structure (pdb:4Y21), AlphaFold (11) Munc13C rat structure prediction. Structures were truncated if needed to fit into specific regions of the maps.
AlphaFold model of Munc13C construct was fitted into the 3D maps using flexible fitting by ISOLDE 1.2 (12) incorporated into ChimeraX (13). Resulted atomic structures have been deposited in the Protein Data Bank under accession number 7T7V for Lateral Munc13C, 7T7X for Upright Munc13C, 7T7C for hexagonal arrangement of Lateral and Upright Munc13C, 7T7R for Upright Munc13C trimer and 7T81 for lateral hexagon surrounded by upright trimers.

SNAREpin assembly distance

In order to estimate maximum distance between synaptic vesicle and plasma membrane at which SNAREpin can assemble we used data from (14). We re-analyzed it in order to relate their results concerning SNAREs artificially anchored to beads to the biologically-relevant case of SNAREs anchored by their trans-membrane domains into apposing bilayers. We concluded that the template complex cannot form at intermembrane separations larger than 10.5 nm, on the following basis: Suppose a maximum of 5 pN membrane opposing force applied to the template complex, the disordered polypeptide has a maximum extension of 6.3 nm calculated from the Marko-Siggia formula for the worm-like chain model of polypeptide (with a persistence length of 0.6 nm). Plus, the distance between two C-terminal anchoring sites on the template complex (4.2 nm), or the size of the template complex in the pulling direction that is considered as a rigid body, the maximum total distance

between the two membranes mediated by a single template complex is 10.5 nm. The minimal distance is determined by the size of the template complex, which is 4.2 nm.

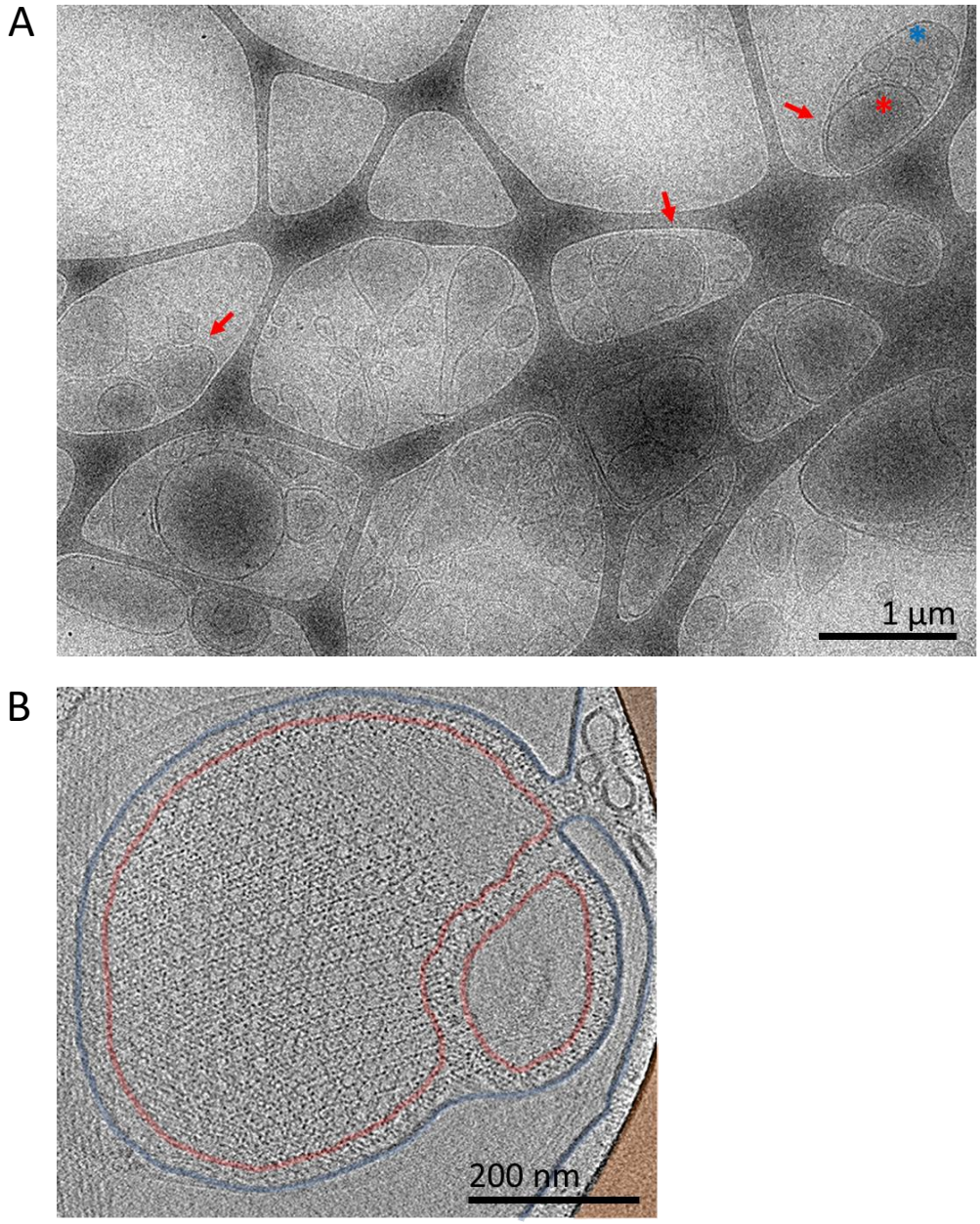

Fig. S1. (A) Low magnification view of sample with Munc13C crystals on the Lacey grid. Multiple sized vesicles are visible with formed crystals (pointed red arrows) with distinct even membranes separation. One of the possible mechanisms of crystal formation is a large unilamellar vesicle (blue star) wrapping around smaller one (red star). (B) Slice through the reconstructed tomogram showing formed crystal between large vesicle (outlined by blue transparent line) that consumed smaller one (approximate membrane is outlined by red transparent line). Brown colored area is carbon from Lacey support.

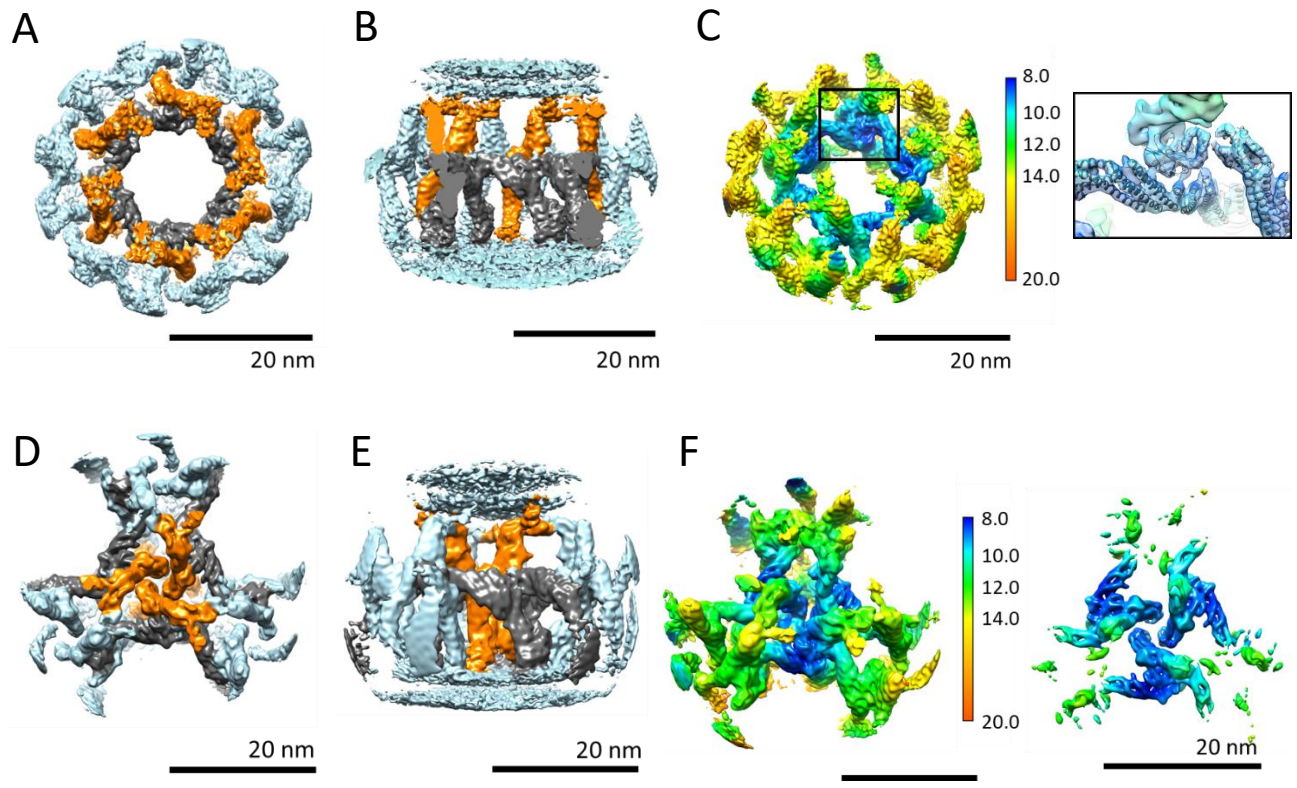

Fig. S2. (A) Top view of 3D reconstruction of the crystal with focus on hexagonal unit ('hexamer cage'), isosurface rendering. (B) Cross-section of the volume through the center of the hexamer cage. The hexagonal assembly of Lateral Munc13C molecules are colored grey, and each such hexagon interacts with six Upright Munc13C molecules (colored in orange). (C) Local resolution heat map showing that the central part of the hexagon is best resolved (8-9 Å resolution), visualizing individual α-helices in this region (zoomed in view of the black square is on the right). Regions closer to membrane are less resolved with 12-14 Å resolution. The color key shows resolution in Å. (D) Top and side (E) views of the crystal 3D reconstruction focused on an Upright Munc13C trimer (colored orange). This trimer is formed by three vertically oriented Munc13C molecules, each interacting with different hexagonal assemblies of laterally oriented Munc13C molecules (colored in grey). (F) Local resolution map (left) of the 3D trimer volume shows similarity in resolution distribution with (C) where only central part is resolved to visible α-helices (shown on the right). Color key once again shows resolution in Å.

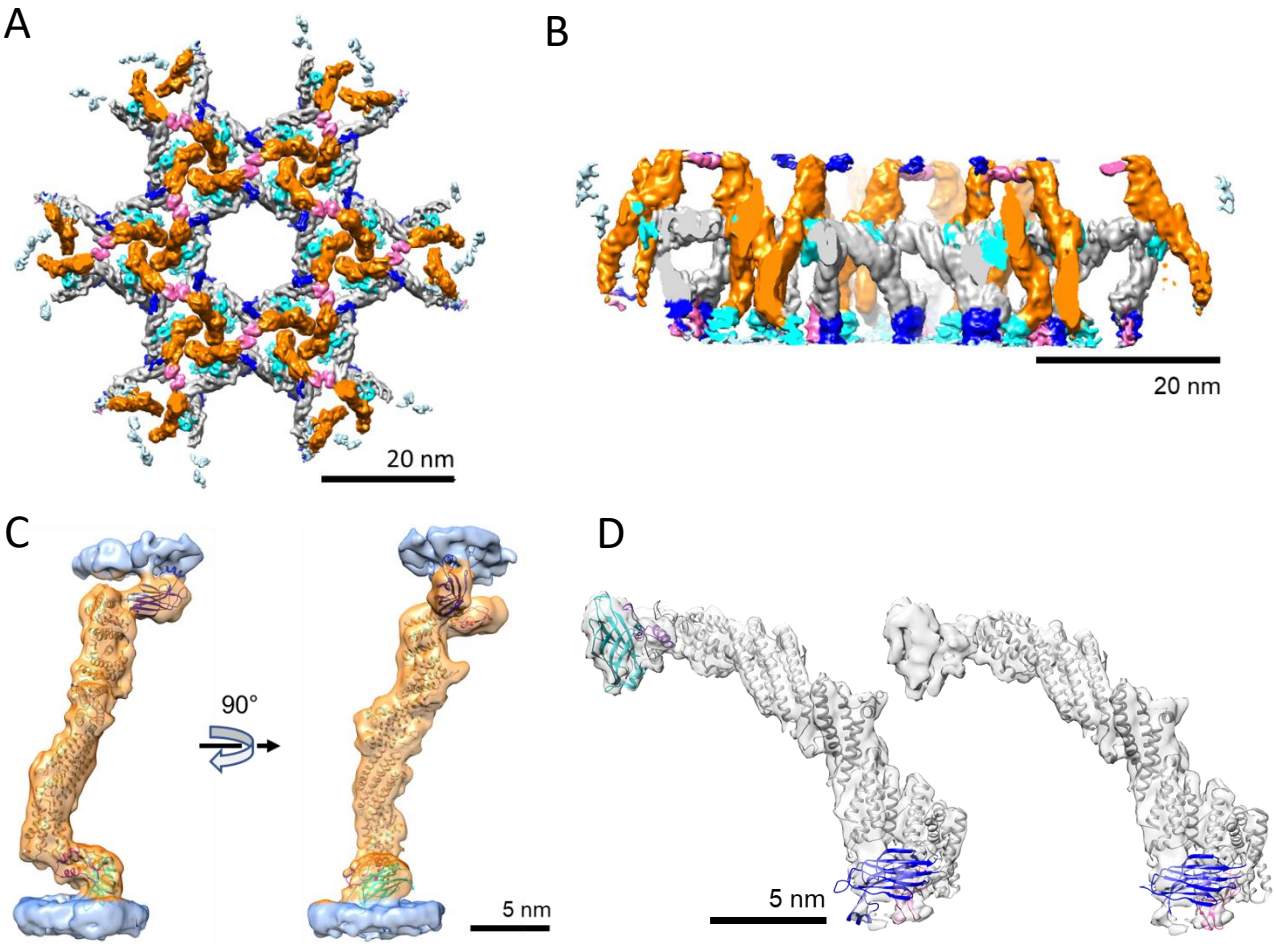

Fig. S3. (A) Top view and (B) cross-section of the volume through the center of the hexagon of a composite 3D map of the crystal, generated by merging high-resolution regions of hexagon-focused and trimer-focused 3D maps (Fig. S2A-C and Fig. S2D-F, respectively); membrane density is not shown for clarity. The map was created in UCSF Chimera by combining one "hexagon" map with six "trimer" maps using the *vop maximum* command. MUN domains of the lateral Munc13C are grey, and upright MUNs are orange; C1 domains colored in pink, C2B are blue and C2C are cyan. Laterally oriented Munc13C molecules forms hexagons via contacts between their C2C domains and MUN domains of neighboring lateral and upright Munc13Cs. Laterally oriented Munc13C molecules interact with only one of the two membranes surrounding the crystal, doing so solely through their C2B/C1 domains. The upright Munc13C crystal conformer forms membrane contacts C2C domain only (not C1) while its MUN domain spans between two membranes such that the C2B domain interacts with the opposite lipid membrane. Note that the laterally oriented and upright oriented Munc13C conformers have opposite polarities with respect to the crystal, such that the C2C domain of the upright conformer contacts the same membrane surface as the C2B/C1 domains of the lateral conformer. (C) Upright Munc13C 3D volume with a fitted structure of the AlphaFold predicted Munc13C model. Volume surface colors are: protein – orange, membrane surface – blue. (D) Lateral Munc13C molecule. *Left* is a fitted structure of the AlphaFold predicted Munc13C model. *Right* is a fitted X-ray crystal structure of C1-C2B-MUN (pdb: 5UE8). Both (C) and (D) composite 3D maps were created in UCSF Chimera by combining two maps from independent, focused 3D classifications using the *vop maximum* command (see Fig. S13). In (C), (D) ribbon colors are: C1 – pink, C2B – blue, MUN – grey, C2C – cyan, C-terminal sequence after C2C (MCT domain) – purple.

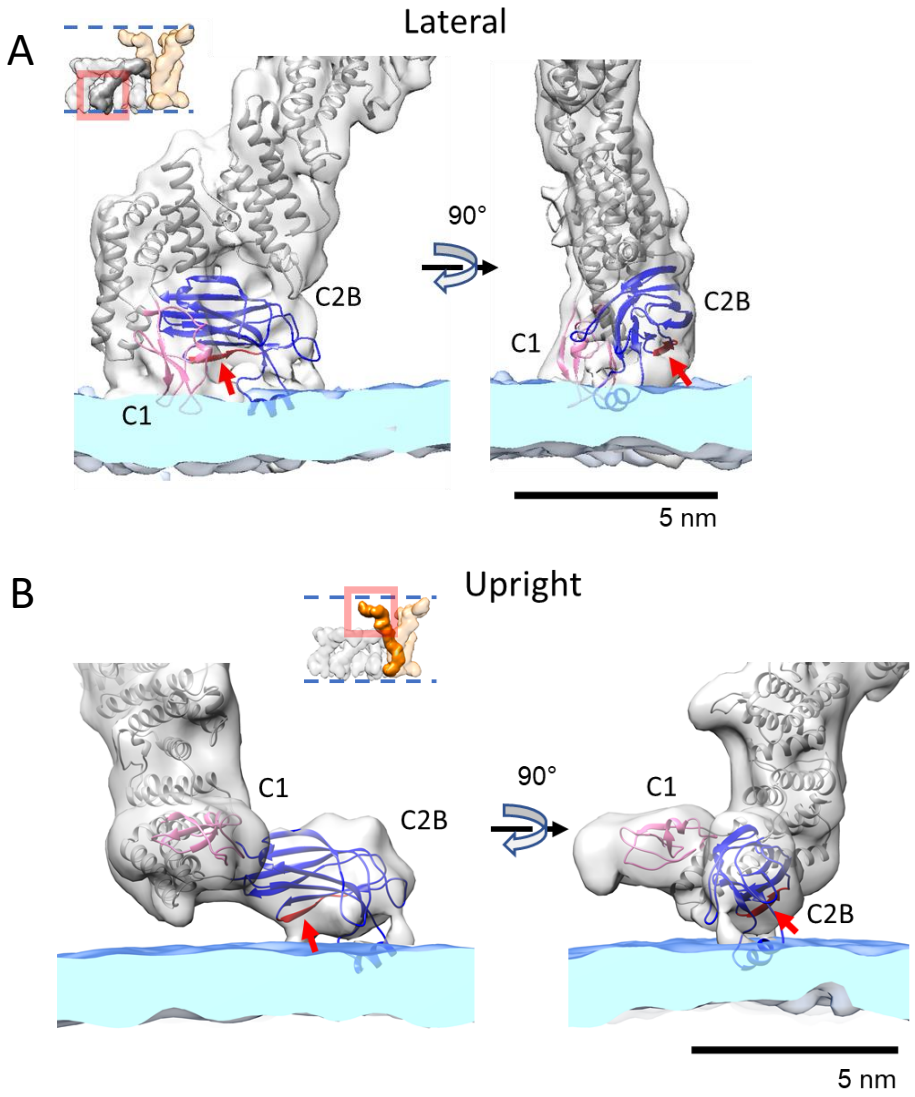

Fig. S4. (A) Lateral Munc13C N-terminal end electron microscopy map (inset shows corresponding location in the crystal) with a fitted Munc13C (AlphaFold) model, shown as a ribbon representation. MUN domain ribbons colored in grey, C1 domain is pink, C2B is blue. Positively a/a rich β-strand (red arrow) are highlighted by red color. Membrane (blue color) density was obtained from the "trimer" map by segmenting out membrane leaflet without proteins and using Gaussian filter with width σ=3. The membrane is positioned at the same level as it is in the experimentally obtained 3D map. In this orientation the Munc13C loop 3 of the C2B domain and two loops of the C1 domain that form the DAG-binding pocket are submerged beneath the bilayer surface, coplanar with the phospholipid heads. The 'polybasic patch'-containing β-strand (red) is oriented parallel to the membrane surface. (B) Upright Munc13C N-terminal end electron microscopy map (inset shows the corresponding location in the crystal) with fitted Munc13C (AlphaFold). The color scheme is identical to (A). The C2B portion of the map is less well resolved, probably due to relatively flexible positioning of the C2B on the membrane; nevertheless, the overall shape of this domain suggests that the orientation is similar to that of the Lateral C2B, such that loop 3 is submerged beneath the bilayer surface, coplanar with the phospholipid heads and the polybasic β-strand (red, red arrow) is in parallel to the membrane surface. The rest of the molecule is oriented differently from the lateral conformation to accommodate the more vertical orientation of the MUN domain (see main text for details).

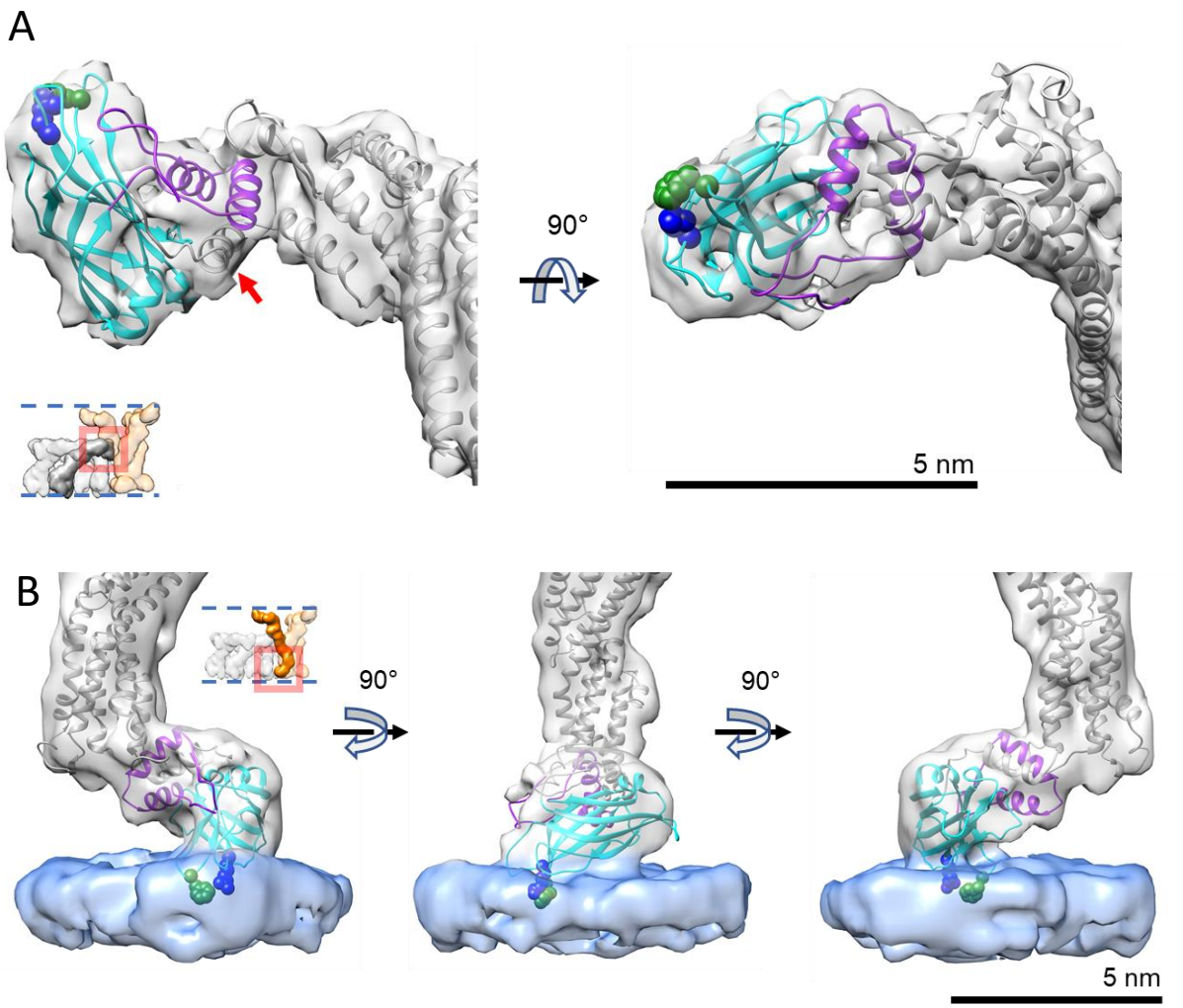

Fig. S5. (A) 3D map of C-terminal region of lateral Munc13C with fitted ribbon structure representation of AlphaFold Munc13C prediction (inset shows corresponding location in the crystal). The AlphaFold prediction overall fits well into the map density; the linker region between MUN and C2C (cyan) is predicted to be α-helical (red arrow). R1598 (blue spheres) and F1658 (green spheres) side chains are shown to visualize the position of the membrane interacting interface of C2C domain. The Munc13 C-terminal domain (MCT, magenta) is represented by two α-helices with unstructured tail. The linker helix (dark grey) and MCT domain form an interface between MUN and C2C domains, which can explain its importance in Munc13 function (15). (B) 3D map of the C-terminal region of Upright Munc13C with fitted ribbon structure representation of the AlphaFold Munc13C prediction (inset shows corresponding location in the crystal); density representing the plane of the phospholipid heads is colored in light blue. Color scheme of ribbon structure representation is similar to (A). Fitting shows that R1598 (blue spheres) and F1658 (green spheres) side chains are submerged into lipid bilayer and overall C2C orientation corresponds well to modelled type I C2 domain interaction with lipid membranes (16).

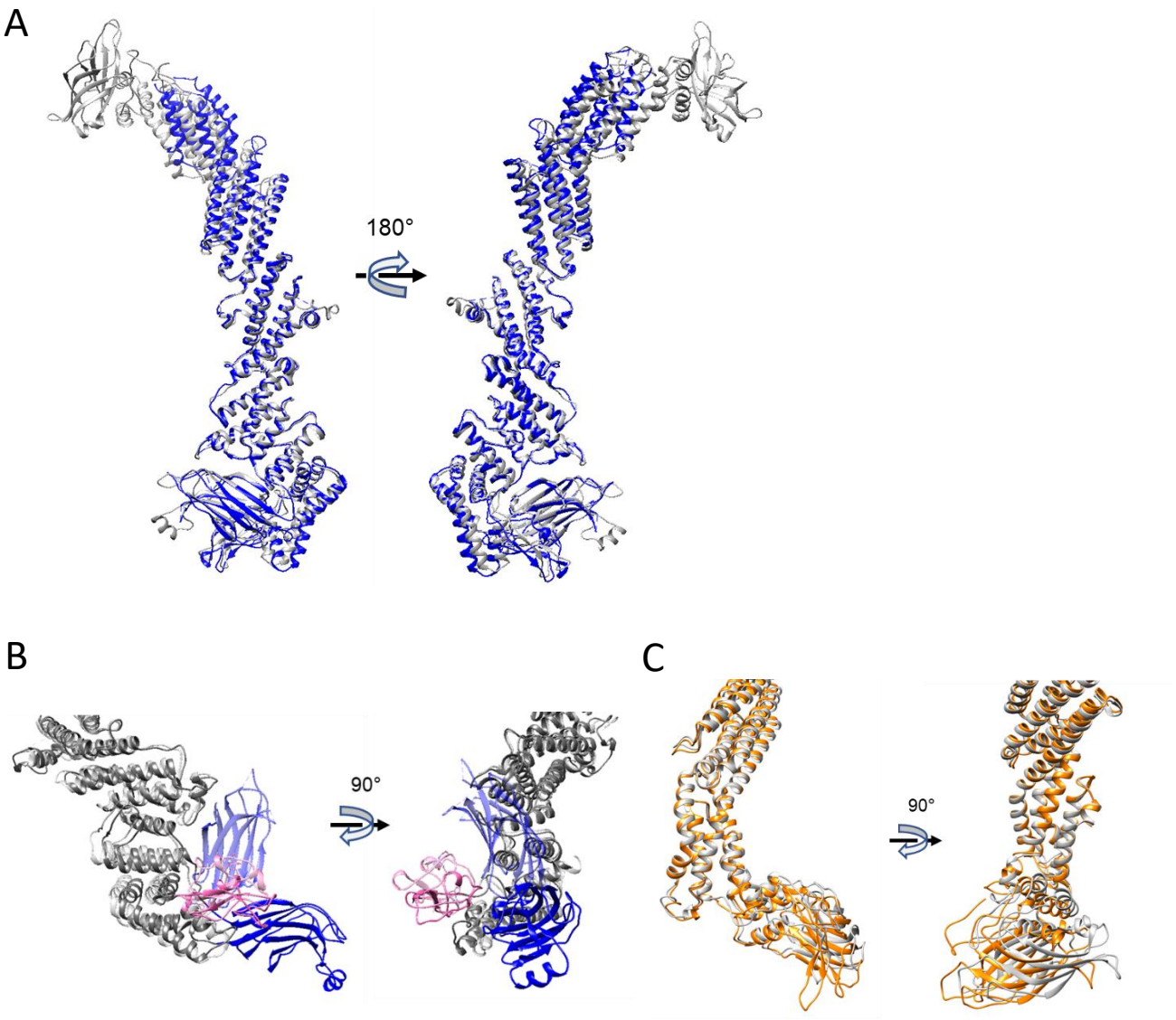

Fig. S6. (A) Ribbon representation of the lateral Muc13C structure colored in grey, aligned with X-ray crystal structure of C1-C2B-MUN (pdb: 5UE8) colored in blue using the N-terminal region (including C2B and C1 domains) for alignment. (B) Superimposed N-terminal region of upright Munc13C and C1-C2B-MUN (pdb: 5UE8, semitransparent) molecules. Alignment by the N-terminal part of MUN domain shows dramatic change in C2B domain orientation relative to C1 and MUN domains. (C) Superimposed C2C regions of lateral (grey) and upright (orange) Munc13C molecules. Alignment by the C-terminal part of MUN domain shows almost identical C2C positioning relative to MUN domain (small deviation in C2C-MCT position probably due to lower resolution in the upright Munc13C C2C region and result loss of fitting accuracy).

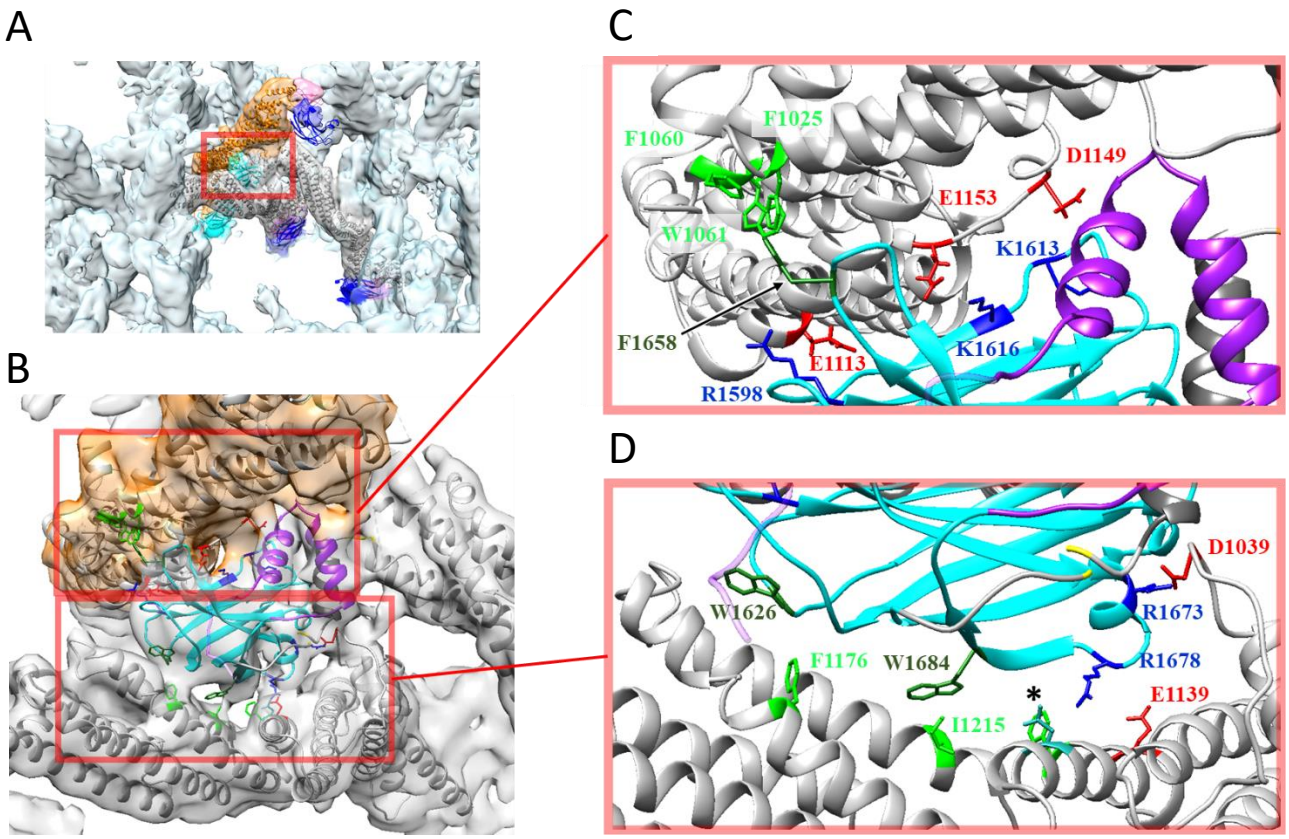

Fig. S7. Support interface between lateral and upright Munc13C molecules. (A) Interface position in the crystal. The support interface is formed between one C-terminal end of a lateral Munc13C molecule and two neighboring Munc13Cs: one lateral and one upright (orange colored). (B) Zoom-in of the red rectangular area from (A). The supporting interface is formed by two interactions: one (top red rectangle) is between C2C (cyan ribbons) and MCT (purple ribbons) domains interacting with an upright MUN domain (grey ribbons in orange colored surface density representation); the second one is between a C2C and the MUN domain of an adjacent lateral Munc13C in the hexagon cage (grey ribbons, lower red rectangle). (C) and (D) zoom-in of corresponding regions, with possible amino acid interactions labeled. Interactions between C2C and the MUN domain of an upright Munc13C (C) utilize the membrane interacting surface of the C2C domain and are mainly an electrostatic in nature, whereas interactions with the neighboring lateral MUN in the hexagon cage (D) likely involve hydrophobic interactions (amino acids on the left side) in addition to electrostatic (amino acids on the right). The latter interaction also covers the Syntaxin-1A binding region ('NF', functionally important amino acids labeled with asterisk), which would make inaccessible for interaction.

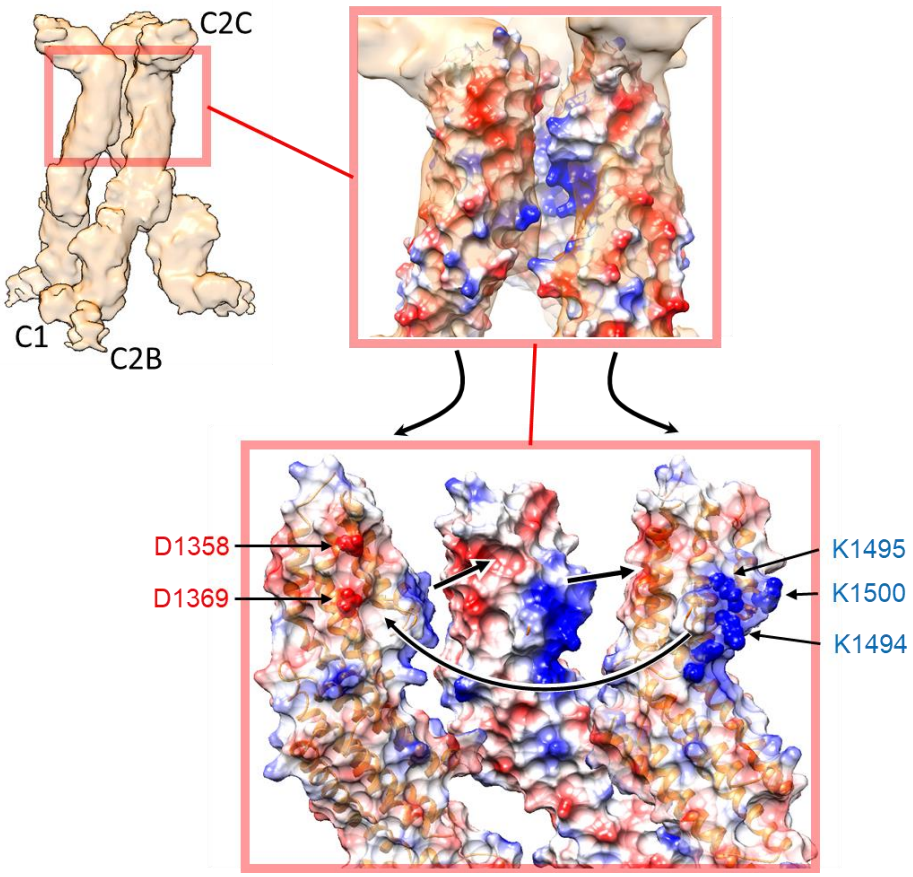

Fig. S8. Upright Munc13C trimer interface. Top left – 3D density surface representation of the trimer oriented with C2C domains up and C1-C2B down. Top left is zoomed-in area with Coulomb surface coloring created by UCSF Chimera showing that this interface is electrostatic in nature. Lower image shows interface opening and possible amino acids contributing to the trimer interface.

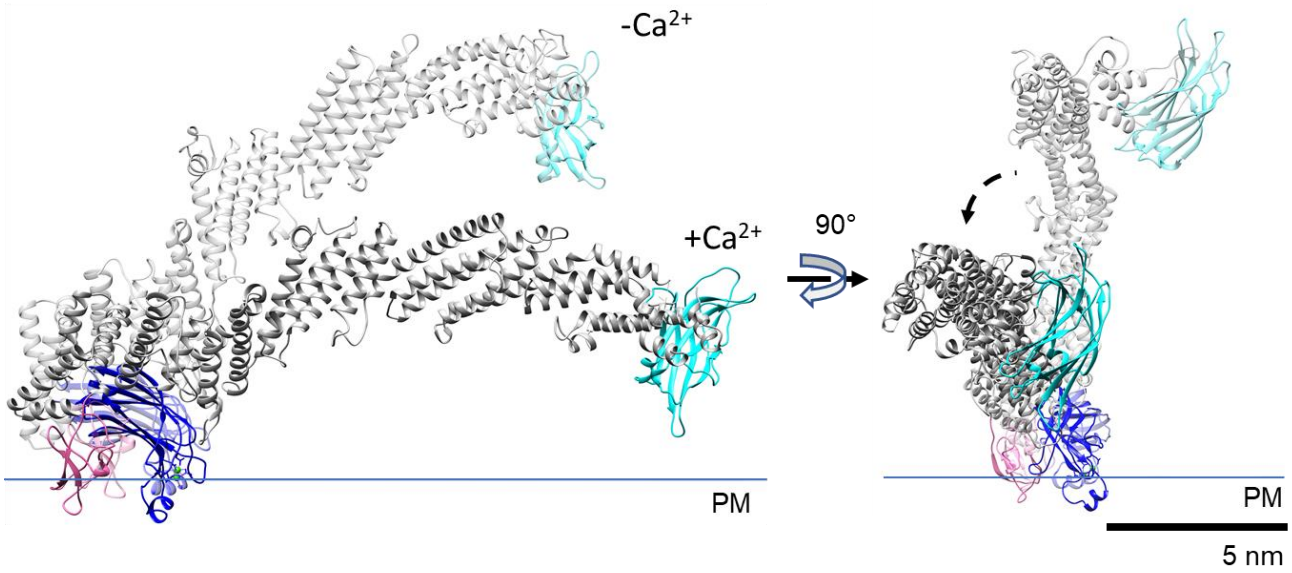

Fig. S9. Model for transition from state 2 to state 3 on the membrane surface (PM). A Ca^{++}-dependent change in the orientation of C2B rotates the attached MUN-C2C domain towards the PM bilayer. The left panel illustrates the proposed rotation from the experimentally-determined lateral geometry (transparent structure, above) to the modelled Ca^{++}-bound and more tilted geometry (colored structure, below) which is based on the known re-orientation of the homologous C2B domain of Synaptotagmin-1 (17-19), which simultaneously inserts loops 1 and 3 into the bilayer upon binding Ca^{++}. This geometry was qualitatively adjusted to attempt to take into account the less hydrophobic loop 1 of Munc13-1 while also maintaining contact between the DAG-binding site of the C1 domain and the bilayer as would be needed to maintain DAG binding in state 3. The right panel shows the view of the model from the C2C side, illustrating that the suggested rotation (maintaining the contacts between C1 and C2B) not only brings MUN-C2C much closer to the PM but also rotates it away from the center of the lateral hexamer cage (which would be to the right in this view). This proposed geometry is only meant to be indicative. As a principal alternative, for example, the simultaneous binding of Ca^{++} and DAG could also disrupt the interface between C1 and C2B, thereby reducing orientational constraints on the now liberated C2B-MUN-C2C unit.

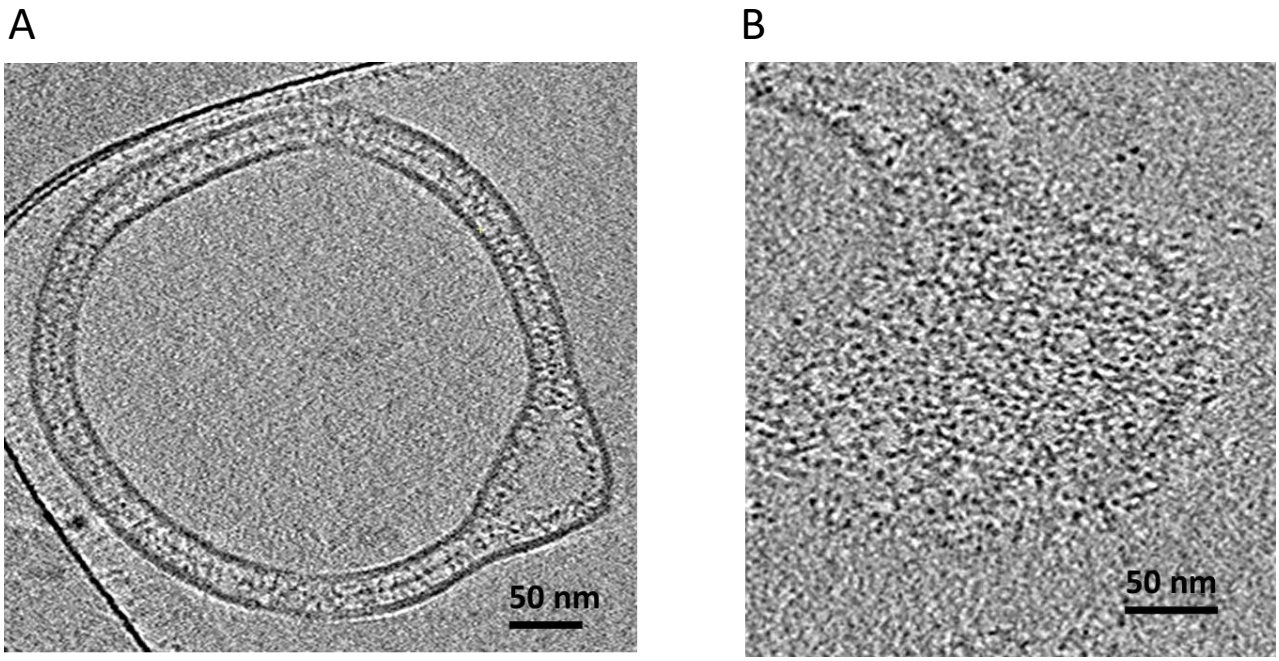

Fig. S10. Representative slices of the reconstructed tomograms of Munc13C crystal formed in the presence of 0.5%mol DAG in the lipid membranes (lipid composition DOPC/PIP2/DAG/DOPS 13.5/6/0.5/80). (A) Cross section of the formed crystal with characteristic protein density between membrane bilayers. (B) Top view of the formed crystal with visible hexagons. Scale bars 50 nm.

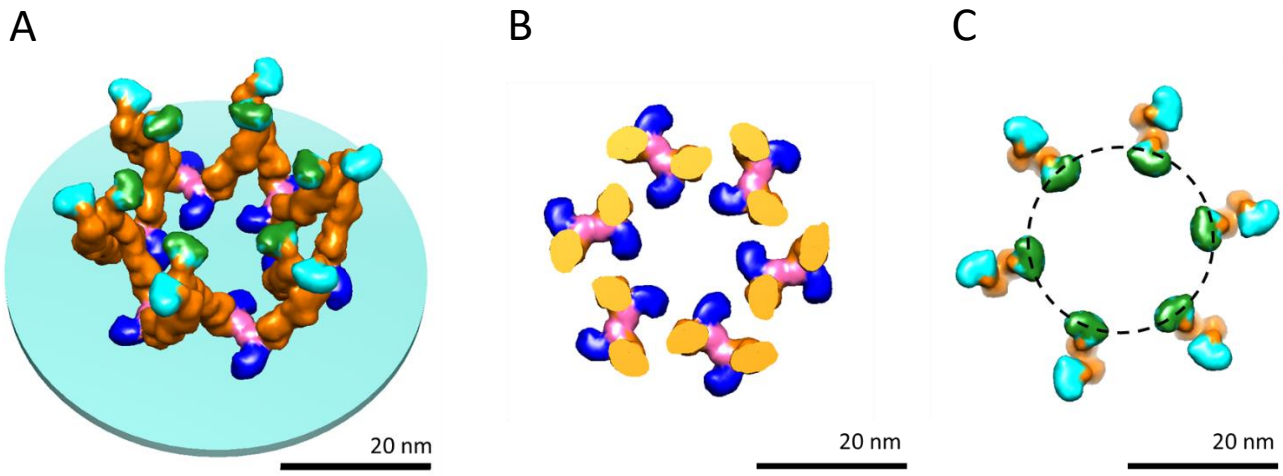

Fig. S11. (A) Oblique view of the hexagonal array of upright dimers model made by removing from the trimers upright Munc13C molecules whose C1 domains are not involved in C1-C1 interactions (see Fig 2). The C1 domain is colored pink, C2B in dark blue, MUN domain in orange and C2C in cyan. (B) View of the hexagonal array as in (A) but showing a horizontal slice focused on the C1/ C2B domains, 5 nm above the 'PM' membrane shown in (A). Domain coloring is the same as in panel (A). (F) Top view of the dimeric hexamer, focusing on the C2C domains. The dashed line represents the edge of a 45 nm vesicle if it were parked in the middle of the trimeric hexamer, bound to the innermost ring C2C domains (green).

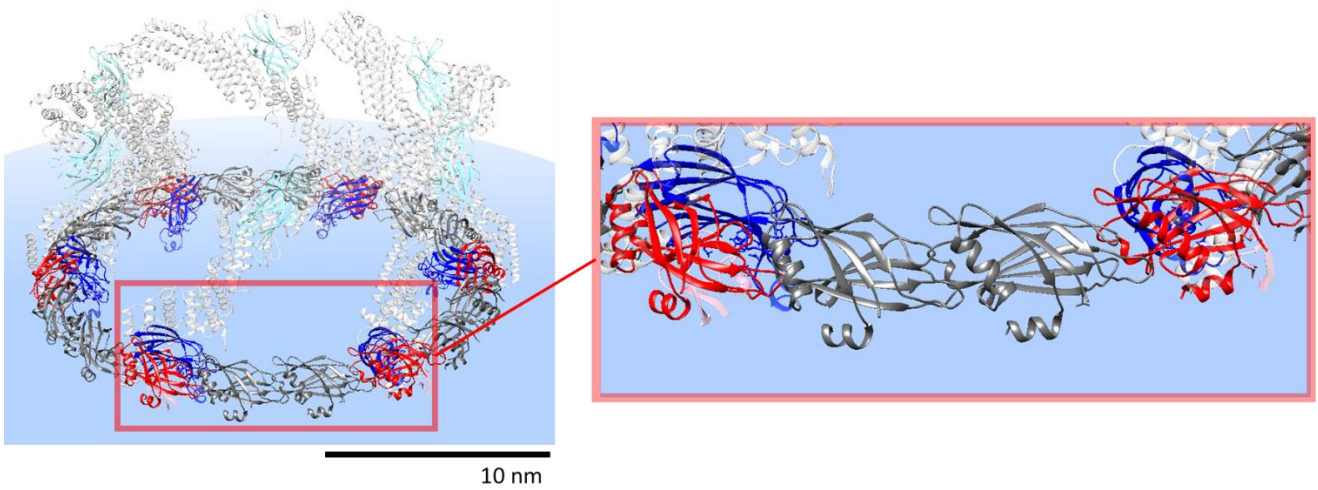

Fig. S12. Superposition of the 18-mer Synaptotagmin C2B ring with the Munc13 C2Bs in the lateral hexamer. Left: semitransparent ribbons represent a lateral hexagon of the Munc13C molecules. C2C domain is colored cyan, MUN domains in grey and C2B are shown in blue. Munc13C's C2B domains positions in lateral hexagon could be described by circle with dimensions similar to 18 subunits Synaptotagmin-1 C2B ring (shown in grey ribbons). Superimposition of these two structures shows an overlap between them and every third Syt1-C2B domain (red ribbons) in the ring is positioned at Munc13C C2B domain location in the lateral hexagon. Right: zoom-in of the area withing the red rectangle.

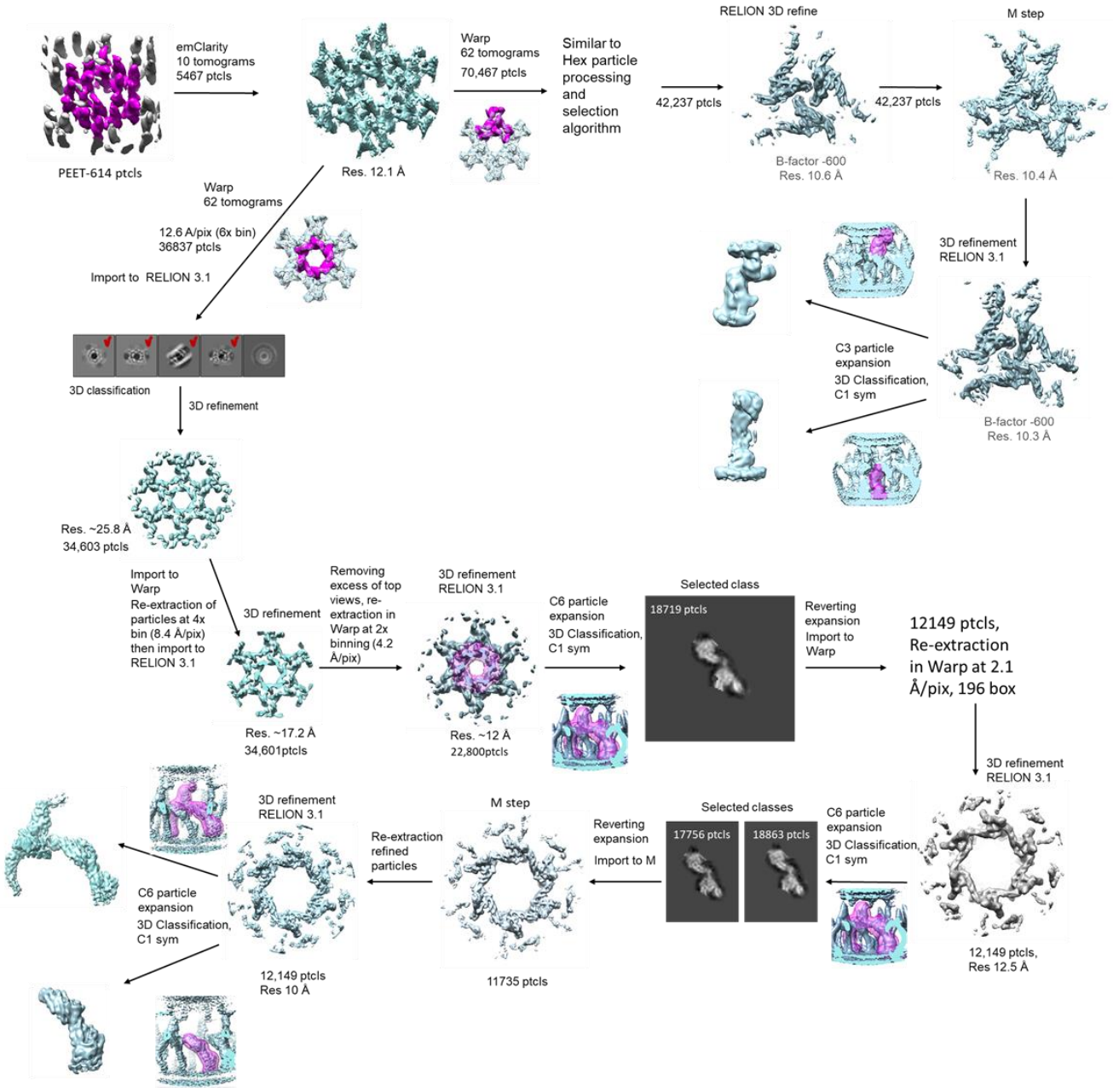

Fig. S13. Schematic of the procedures used for subtomogram refinement and 3D reconstruction. Masks are shown in semitransparent purple. Areas used for templated particle picking process are colored in magenta.

Movie S1 (separate file). Transition between upright and lateral states of Munc13C.

Movie S2 (separate file). Transition between upright hexamer and lateral hexamer of Munc13C.

SI References

1. S. Q. Zheng *et al.*, MotionCor2: anisotropic correction of beam-induced motion for improved cryo-electron microscopy. *Nat Methods* **14**, 331-332 (2017).
2. J. R. Kremer, D. N. Mastronarde, J. R. McIntosh, Computer visualization of three-dimensional image data using IMOD. *J Struct Biol* **116**, 71-76 (1996).
3. P. Gilbert, Iterative methods for the three-dimensional reconstruction of an object from projections. *J Theor Biol* **36**, 105-117 (1972).
4. B. A. Himes, P. Zhang, emClarity: software for high-resolution cryo-electron tomography and subtomogram averaging. *Nat Methods* **15**, 955-961 (2018).
5. D. Nicastro *et al.*, The molecular architecture of axonemes revealed by cryoelectron tomography. *Science* **313**, 944-948 (2006).
6. D. Tegunov, P. Cramer, Real-time cryo-electron microscopy data preprocessing with Warp. *Nat Methods* **16**, 1146-1152 (2019).
7. S. H. Scheres, RELION: implementation of a Bayesian approach to cryo-EM structure determination. *J Struct Biol* **180**, 519-530 (2012).
8. T. A. M. Bharat, C. J. Russo, J. Lowe, L. A. Passmore, S. H. W. Scheres, Advances in Single-Particle Electron Cryomicroscopy Structure Determination applied to Sub-tomogram Averaging. *Structure* **23**, 1743-1753 (2015).
9. D. Tegunov, L. Xue, C. Dienemann, P. Cramer, J. Mahamid, Multi-particle cryo-EM refinement with M visualizes ribosome-antibiotic complex at 3.5 A in cells. *Nat Methods* **18**, 186-193 (2021).
10. E. F. Pettersen *et al.*, UCSF Chimera--a visualization system for exploratory research and analysis. *J Comput Chem* **25**, 1605-1612 (2004).
11. J. Jumper *et al.*, Highly accurate protein structure prediction with AlphaFold. *Nature* **596**, 583-589 (2021).
12. T. I. Croll, ISOLDE: a physically realistic environment for model building into low-resolution electron-density maps. *Acta Crystallogr D Struct Biol* **74**, 519-530 (2018).
13. E. F. Pettersen *et al.*, UCSF ChimeraX: Structure visualization for researchers, educators, and developers. *Protein Sci* **30**, 70-82 (2021).
14. J. Jiao *et al.*, Munc18-1 catalyzes neuronal SNARE assembly by templating SNARE association. *Elife* **7**, e41771 (2018).
15. M. Padmanarayana *et al.*, A unique C2 domain at the C terminus of Munc13 promotes synaptic vesicle priming. *Proc Natl Acad Sci U S A* **118** (2021).

16. A. H. Larsen, M. S. P. Sansom, Binding of Ca(2+)-independent C2 domains to lipid membranes: A multi-scale molecular dynamics study. *Structure* **29**, 1200-1213 e1202 (2021).
17. W. Kuo, D. Z. Herrick, J. F. Ellena, D. S. Cafiso, The Calcium-Dependent and Calcium-Independent Membrane Binding of Synaptotagmin 1: Two Modes of C2B Binding. *Journal of Molecular Biology* **387**, 284-294 (2009).
18. J. Bai, W. C. Tucker, E. R. Chapman, PIP2 increases the speed of response of synaptotagmin and steers its membrane-penetration activity toward the plasma membrane. *Nat Struct Mol Biol* **11**, 36-44 (2004).
19. E. Hui, J. Bai, E. R. Chapman, Ca2+-triggered simultaneous membrane penetration of the tandem C2-domains of synaptotagmin I. *Biophys J* **91**, 1767-1777 (2006).